

Surpassing the quarter-wave limit for thin film perfect absorbers with epsilon-near-zero media

Ben Johns*, Shashwata Chattopadhyay & J. Mitra*

School of Physics, Indian Institute of Science Education and Research, Thiruvananthapuram, India 695551

*ben16@iisertvm.ac.in, j.mitra@iisertvm.ac.in

ABSTRACT: A conventional dielectric optical coating supports Fabry–Perot resonances if the thickness is at least a quarter-wavelength of the incident radiation. We show that for light incident obliquely, a low loss epsilon-near-zero (ENZ) thin film coating on a highly metallic substrate can support resonant interferences leading to perfect absorption, well below the quarter-wave thickness limit. The physical mechanism is based on evanescent fields in the ENZ medium, which is distinct from previous demonstrations of ultrathin-film interference achieved only on weakly metallic substrates and accompanied by significant loss. We also explain previously observed absorption features in metal-backed ENZ thin films based on this phenomenon and reveal the unique role of ENZ response in achieving perfect absorption using low loss materials. These readily configurable *perfect* absorbers are not only easy to engineer at surfaces and interfaces but the underlying design principles and the predictive model elucidated here will be of interest in fundamental optics research and amenable for functional applications.

Dielectric thin-film interference gives rise to captivating effects such as the prismatic colors seen on an oil film on a wet surface or the iridescence of light reflected from a soap bubble. These phenomena originate from Fabry-Perot (FP) type resonances within thin films where multiple reflections interfere, with the resulting intensity or color determined by the accumulated optical phases. With negligible losses, the interface phase shifts (i.e. on reflection or transmission) are typically either 0 or π , and resonant interference conditions are determined by the phase accumulated during propagation. For example, the simplest dielectric anti-reflection coating has a thickness $d = \lambda/4n$ that provides the necessary π phase shift for destructive interference of reflected waves, where λ is the operating wavelength and n is the refractive index [1]. Such a ‘quarter-wave thick’ film placed on an opaque substrate then absorbs incident light completely since both reflection and transmission are simultaneously inhibited. This property of metal-backed, asymmetric FP resonators has found myriad applications as perfect absorbers, e.g. in cavity-enhanced optoelectronic devices such as photodetectors and modulators [2,3].

The bulky nature of wavelength-scale thin-film components makes them ill-suited for integrated optics applications, where absorbers based on artificially engineered metamaterials and plasmonic nanostructures have gained increasing attention due to their deep sub-wavelength dimensions [4]. Nevertheless, thin film-based planar devices based on homogeneous media are scalable, cost-effective and free from complex nanoscale engineering. Therefore, it is interesting to explore conditions where they may be utilized at ultrathin ($d \ll \lambda$) dimensions. For a thin film on a perfect electric conductor (PEC) substrate, no absorption resonance exists below the quarter-wave thickness at normal incidence [5]. To overcome this thickness limit of perfect absorption (PA), the primary dependence on film thickness for phase accumulation must be overcome; this requires interface phase shifts that deviate significantly from the lossless case. Such resonant interferences exploiting non-trivial interface phase shifts have been demonstrated in ultrathin films by introducing weakly reflecting (i.e. absorbing) metal substrates [5-7], metamaterial mirrors [8] or perfect magnetic mirrors [9] instead of PECs. The reduced film thickness positively impacts fabrication and material costs making it attractive for applications in coloring/filtering, enhanced photovoltaic absorption, and infrared absorbers/emitters [10-15]. However, the requirement of absorbing metallic or metamaterial substrates limits their use with low cost metals such as Al and particularly at infrared wavelengths where conventional metals (e.g. Au, Ag) behave increasingly like PECs. Further, reduced absorber volumes require highly absorbing (lossy) thin films or substrates, adding further design constraints. Parasitic absorption in metal substrates may also be unfavorable for energy conversion applications.

In recent years, there has been great interest in the optical response of structures with a vanishing real part of permittivity, called epsilon-near-zero (ENZ) media [16,17]. ENZ materials offer strong light-matter interactions and show exciting effects such as super-coupling [18,19], nanoscale field confinement/enhancement [20-24], emission control [21,25,26] and extreme non-linearities [17,27-31]. Strong absorption in ENZ films is a key to its applications in nanophotonic modulators [32] and ultrafast signal processing [33]. Interestingly, (polarization-dependent) PA has been predicted in low loss, ultrathin ENZ layers on PEC substrates at *oblique* incidence i.e. a non-zero angle of incidence [34-36]. This has been explained by various effects such as coherent cancelling [34], effective impedance matching [35] and critical coupling [37,38]. However, in light of the ultrathin-film interference picture, it is not clear how the necessary non-trivial phase shifts are achieved with a PEC substrate *and* a low loss ultrathin layer. These effects motivate a question of fundamental interest in the context of thin film perfect absorbers: how is the quarter-wave limit surpassed in these PEC-backed, low loss ENZ layers?

Here, we elucidate the conditions for resonant interferences in ultrathin, PEC-backed, low loss films, which lead to perfect absorption well below the quarter-wave limit. The key to this phenomenon is the below unity refractive index ($n < 1$) of the thin film that causes total external reflection (TER) of light

incident obliquely at the air–thin-film interface [39–41]. The angle-dependent reflection phase due to TER provides the required interface phase shifts to completely suppress reflection by destructive interference of light reflected from the top and bottom interfaces of the thin film. Importantly, this restricts the effect to angles above the critical angle for TER at the top interface. We numerically verify these effects in a transparent conducting oxide ENZ thin film at near-IR wavelengths, where strong absorption restricted to the $n < 1$ spectral regime is demonstrated. Finally, we show that the low loss PA is enabled by strong field enhancements due to the ENZ response in low n media, mitigating the need for highly lossy materials as ultrathin absorbers.

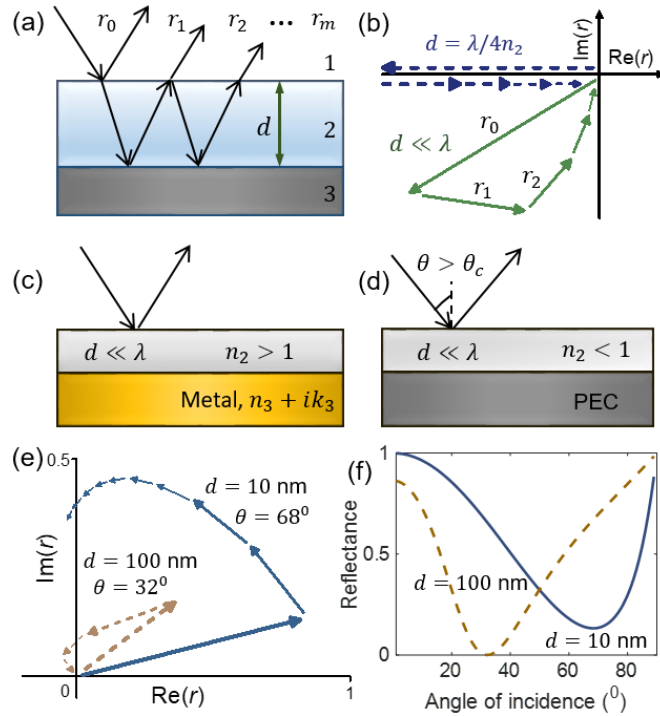


Figure 1: (a) Schematic of a thin film on an opaque substrate showing multiple reflections and resulting partial waves r_m . (b) Phasor diagram of partial waves in a PEC-backed, quarter-wave resonator ($d = \lambda/4n_2$, dashed arrows) and an absorbing metal-backed, ultrathin resonator ($d \ll \lambda$, solid arrows) (c) When the opaque substrate is an absorbing metal, phase shifts at the film-substrate interface allow resonances for $d \ll \lambda$. (d) Resonant absorption in a PEC-backed ultrathin resonator requires non-trivial phase shifts at the air-film interface, which is achieved when $n_2 < 1$ for angle of incidence greater than the critical angle θ_c (e) Phasor diagrams for the case in (d) with $n_2 = 0.45 + 0.15i$ for $d = 100 \text{ nm}$ (dashed), 10 nm (solid) (see text) (f) Corresponding reflectance goes to zero for 100 nm film and ≈ 0.1 for 10 nm film at their respective angles where phasor sum approaches the origin.

Figure 1(a) shows the schematic of a perfect absorber, with light incident from air ($n_1 = 1$) onto a thin film of refractive index $n_2 + ik_2$, of thickness d on an opaque substrate ($n_3 + ik_3$). The reflectance of the system $R = |r|^2$ can be written as [42];

$$r = \frac{r_{12} + r_{23}e^{2i\delta}}{1 + r_{12}r_{23}e^{2i\delta}} = \sum_{m=0}^{\infty} r_m \quad (1)$$

where r_{ij} is the Fresnel reflection coefficient for incidence from medium i to j , $\delta = k_{z2}d$ and $k_{z2} = k_0\sqrt{\epsilon_2 - \epsilon_1 \sin^2 \theta}$ is the wave vector component normal to the interface in the thin film, ϵ is the complex permittivity, k_0 is the free space wave number and θ is the angle of incidence from air. The reflection coefficient r may also be expressed as the coherent sum of infinitely many partial waves r_m [Fig 1(a)]. r_0 corresponds to the partially reflected wave from the first interface ($= r_{12}$) and $r_m = (1 - r_{12}^2)r_{23}^m r_{21}^{(m-1)} e^{2mi\delta}$ ($m \geq 1$) correspond to those emerging from the cavity after m roundtrips. These partial waves may be conveniently represented as phasors in the complex plane [$\text{Re}(r)$, $\text{Im}(r)$] [5,6]. The dashed arrows in Fig. 1(b) show the phasors for a PEC-backed conventional ($n_2 > 1$) quarter-wave thick absorber [6]. At normal incidence, the first reflection r_0 has a phase shift of π (rarer to denser medium) and its phasor points to the left, which is cancelled out by the remaining partial waves that acquire π phase each from the PEC substrate reflection and a roundtrip in the film. The corresponding phasors then point to the right and their trajectory ends up at the origin, giving $R = |r|^2 = 0$. If instead of a perfectly reflecting substrate, an absorbing material such as Au at visible frequencies is combined with a lossy thin film, the phasors are no longer horizontal and the reflection phase at the film-substrate interface differs significantly from π , allowing the partial waves to cancel out r_0 even when $d \ll \lambda$ [Fig 1(c)]. Solid arrows in Fig. 1(b) shows the phasor trajectory of such a system [5] with parameters $d = 10$ nm, $n_2 = 4.3 + 0.7i$ and $n_3 = 0.44 + 2.24i$ at $\lambda = 532$ nm, which returns to the origin tracing out a loop, corresponding to $d \approx \lambda/12n_2$.

In order to achieve PA in ultrathin films backed by PECs (which impart π phase), it is necessary to obtain non-trivial phase shifts at the *first* interface i.e. the air-film interface. For normal incidence at a lossless interface with $n_1 < n_2$, for e.g. air-glass, r_{12} is a negative real number determined by the optical constants with a fixed phase of π . Even for highly absorbing dielectrics where r_{12} becomes complex, the phase deviates by less than $\sim 10^0$ from the lossless case [7,43]. However, if $n_1 > n_2$, light can undergo total internal reflection at oblique incidence. In this case, r_{12} becomes complex above the critical angle $\theta_c = \sin^{-1} n_2/n_1$, signifying the presence of evanescent waves in the rarer medium, and above θ_c it imparts an angle-dependent reflection phase varying between 0 to π [42]. In most applications where $n_1 = 1$, this cannot be achieved with conventional dielectrics ($n_2 > 1$). However, low index media such as ENZ or near-zero-index (NZI) materials offer refractive indices well below 1 [Fig 1(d)] within restricted spectral

windows [16,44] wherein light undergoes TER at their surfaces [39,41]. This is demonstrated by the phasor diagrams in Fig. 1(e) for p -polarized light of $\lambda = 532$ nm incident on a PEC-backed low-index layer with $n_2 = 0.45 + 0.15i$. For $d = 100$ nm ($\approx \lambda/12n_2$), the phasors return back to the origin at incident angle $\theta = 32^\circ$ ($> \theta_c = 27^\circ$). If $d = 10$ nm ($\approx \lambda/120n_2$), the reflectance reaches a minimum (≈ 0.1) at $\theta = 68^\circ$. The corresponding numerically evaluated total reflectance for both thicknesses are plotted against θ in Fig. 1(f) showing respective minima at the angles where the phasor sum reaches closest to the origin. Notably, in contrast to the highly absorbing 10 nm layer in Fig. 1(b), it takes many more roundtrips for the partial waves to converge to the final reflectance for the low-loss 10 nm layer in Fig. 1(e), a marker of the low loss nature of absorption that will be discussed later.

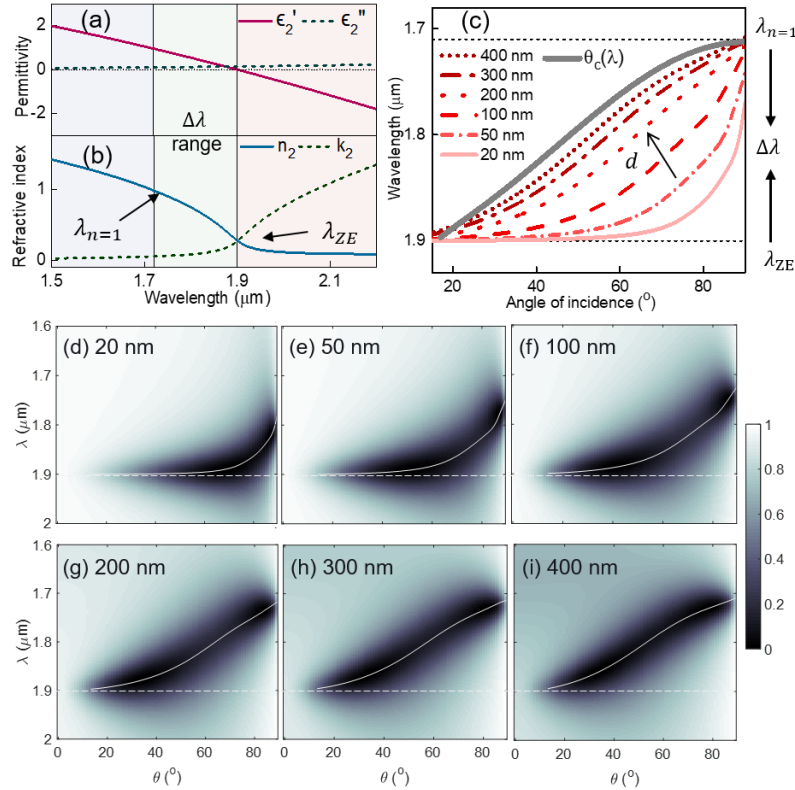


Figure 2 (a) Real (ϵ'_2) and imaginary (ϵ''_2) parts of ENZ medium permittivity. $\epsilon'_2 = 0$ at $\lambda_{ZE} = 1900$ nm (b) Corresponding real (n_2) and imaginary (k_2) parts of refractive index $n_2 + ik_2 = \sqrt{\epsilon_2}$. $n_2 = 1$ at $\lambda_{n=1} \approx 1700$ nm. Vertical lines demarcate the dielectric $\Delta\lambda$ range between $\lambda_{n=1}$ and λ_{ZE} where $n_2 < 1$. (c) Dispersion relations of transverse magnetic modes in ENZ on Au system for varying ENZ thickness d from 400 to 20 nm, with the arrow showing direction of increasing d . The modes are confined to angles above the air-ENZ critical angle θ_c within $\Delta\lambda$ range. (d-i) Reflectance maps of the ENZ on Au system in the $\lambda - \theta$ plane for p -polarized light showing agreement with the dispersion relations in (c) overlaid as solid lines.

A distinct advantage of the proposed mechanism is that it does not require engineered metamaterials or resonant nanostructures to achieve PA. To illustrate the potential effects in continuous media, we analyze a low loss ENZ on metal substrate (ENZ:M) in the IR. The material permittivities $\epsilon_2(\omega)$ and $\epsilon_3(\omega)$ are described by those of CdO and Au for the ENZ and the metal as outlined in Supplementary section 1 [45]. For the model parameters, the ‘zero-epsilon wavelength’ (λ_{ZE}), where $\text{Re}(\epsilon_2) = 0$ lies at $\lambda_{ZE} = 1900$ nm (Fig 2(a)). Fig. 2(b) shows that $n_2 \approx 0.3$ at λ_{ZE} and increases towards lower λ , reaching 1 at $\lambda_{n=1} \approx 1700$ nm. In the wavelength window $\Delta\lambda$ between λ_{ZE} and $\lambda_{n=1}$, the thin film is a dielectric with $n_2 < 1$ [46], where total external reflection becomes possible. Fig. 2(c) plots the dispersion relations for transverse magnetic modes in the ENZ:M system for varying d (see Supplementary section 2 for details of numerical calculations). The dispersions are limited on the long wavelength side by λ_{ZE} , above which the layer becomes metallic i.e. $\epsilon'_2 < 0$, and on the short wavelength side by $\lambda_{n=1}$. Figs. 2(d-i) show the reflection maps of p -polarized light as a function of incident angle and wavelength, evidencing well-defined regions of strong absorption (low reflectance) in the darker regions, which closely follow the corresponding dispersion (solid lines). Figure S1 (Supplementary section 3) shows the reflectance vs θ plots for the various thicknesses at their respective PA wavelengths that vary between 1850 – 1900 nm for decreasing d , and also at $\lambda = 1800$ nm. Evidently reflectance goes to zero at the PA points and reaches a non-zero minima (reflectance ~ 0.2) at other wavelengths. Importantly, the variation with angle is not sharp thereby allowing for reasonably high absorption with wide angular distribution and spectral range. For comparison, figure S2 in Supplementary section 3 plots the reflectance spectra for CdO on a PEC demonstrating a close match with the CdO on Au data above, indicating that Au is fairly well approximated by a PEC in the investigated wavelength range [47]. Since the thickest film is 400 nm ($< \lambda/4$), the modes evidenced above are not thin film FP modes, which appear at shorter wavelengths (Supplementary section 4). Furthermore, the wavelength-dependent critical angle, $\sin \theta_c(\lambda) = n_2(\lambda)$, overlaid on the dispersion relations (grey solid line in Fig 2(c)) shows that the dispersions lie to its right irrespective of the film thickness, i.e. the modes are supported only when light undergoes external reflection at the ENZ surface. The dispersion profiles for larger thicknesses nearly lie on $\theta_c(\lambda)$ and are clearly limited by it (Supplementary section 5). The critical angle approaches 90° as n_2 approaches 1 (at $\lambda_{n=1}$) and the radiative modes vanish at larger values of refractive index below $\lambda_{n=1}$. It may be pointed out that strong absorption in polaritonic ENZ films on reflecting substrates [36,48,49] has widely been interpreted in terms of radiative ENZ modes called Berreman modes [50-53]. However, the dispersions here are different from that of surface polariton modes supported by an ENZ thin film (supplementary section 6) whose dispersion in the radiative regime is not bounded at lower wavelengths.

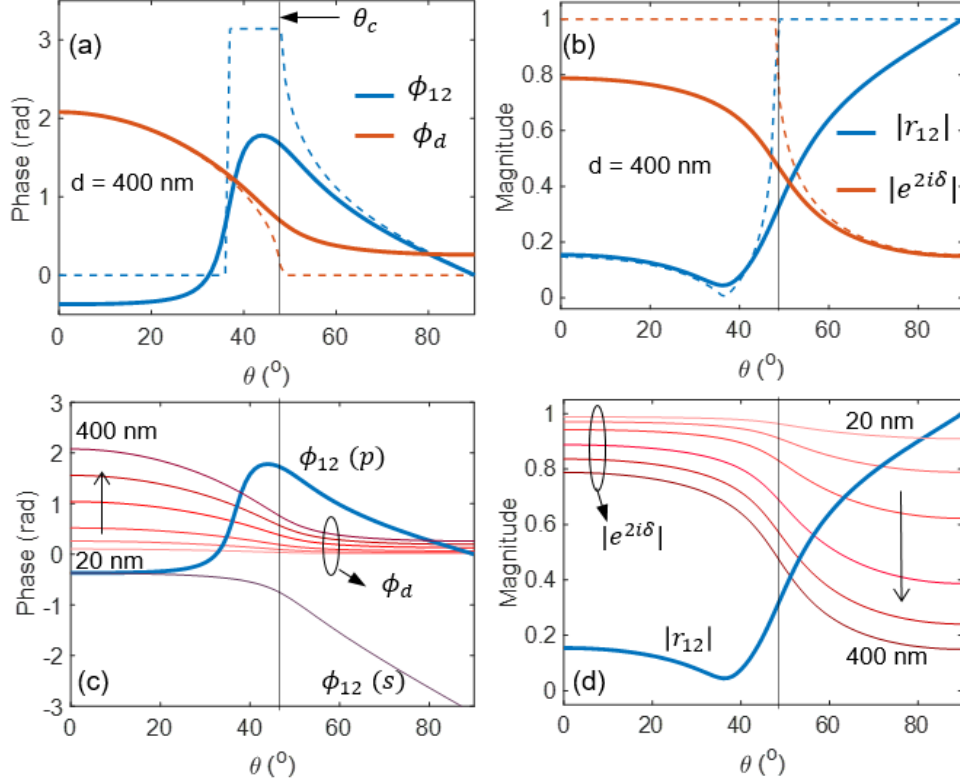


Figure 3 (a) Phase changes on reflection at Air – ENZ interface ϕ_{12} (blue lines), and propagation in ENZ layer ϕ_d (orange lines) versus incident angle θ . (b) Magnitude of reflected wave at Air – ENZ interface (blue) and attenuation over a round trip in the film (orange) vs θ . Plots in (a) and (b) are calculated for p -polarized light with $d = 400$ nm. Dashed lines show the lossless ENZ case where the effects of total external reflection are more pronounced. (c) ϕ_{12} for s and p polarizations and ϕ_d for varying d showing that the phases match only for p -polarized light. (d) Magnitude of external reflection $|r_{12}|$ and wave attenuation in the ENZ layer $|e^{2i\delta}|$ for varying d . The exponential dependence of attenuation on d allows tailoring the resonant angle where the magnitude of external reflection matches the magnitude of attenuated wave in ENZ layer. All calculations are done at $\lambda = 1800$ nm.

To understand the origin of these unique modes in the ENZ regime, we write the three medium reflection coefficient in eqn.1 in the form $r = \frac{r_{12} - e^{2i\delta}}{1 - r_{12}e^{2i\delta}}$ by setting $r_{23} = -1$, corresponding to a PEC substrate [42]. Here, $e^{2i\delta}$ gives the phase advance (and attenuation) for a round trip in the film. For strong absorption, we require that the terms in the numerator of r cancel each other, giving two conditions to be satisfied simultaneously viz. $|r_{12}| \approx |e^{2i\delta}|$ and a phase difference ≈ 0 [11]. Physically, this signifies complete destructive interference between the reflected wave at the first interface and the resultant of the partial waves originating from the thin film (Supplementary section 7, 8). Figure 3(a) plots the phases of

r_{12} (ϕ_{12} , reflection phase shift at the air-ENZ interface) and $e^{2i\delta}$ (ϕ_d , propagation phase in the film) for ENZ:M with $d = 400$ nm at $\lambda = 1800$ nm lying in the $\Delta\lambda$ range (solid lines). For ideal lossless ENZ (dashed lines), ϕ_{12} varies continuously in the range 0 to π above θ_c . On the other hand, $\phi_d = 2 \operatorname{Re}(k_{z2})d$ is non-zero at low angles ($< \pi$ as $d < \lambda/4n_2$), and falls to zero above θ_c . This indicates that the phase shifts determining resonant interference conditions originate dominantly from the reflection phase at the air-ENZ interface, in contradistinction to conventional FP resonances. Fig 3(b) plots the variation in magnitudes of $|r_{12}|$ and $|e^{2i\delta}|$ for real and lossless ENZ. In the absence of loss, $|r_{12}|$ rises up to unity at θ_c (dashed blue line) while $|e^{2i\delta}| = e^{-2 \operatorname{Im}(k_{z2})d}$ has unit magnitude below θ_c and drops off sharply above it as $\operatorname{Im}(k_{z2})$ becomes non-zero. Together, Fig 3(a, b) show that r will be minimum near θ_c corresponding to an optimal match between the magnitudes and phases for $d = 400$ nm, in agreement with its dispersion profile in Fig 2(c) that lies close to $\theta_c(\lambda)$ throughout the $\Delta\lambda$ range. Note that these features are generally valid for wavelengths where external reflection occurs i.e. in the $\Delta\lambda$ window.

In order to explain the thickness and polarization dependence in Fig. 2, ϕ_{12} for both s and p polarizations at $\lambda = 1800$ nm are plotted along with ϕ_d for d in the range $20 - 400$ nm in Fig. 3(c). Evidently, ϕ_{12} for s -polarized light cannot match ϕ_d for any thickness in the investigated range, explaining why interferences effects are observed only for p -polarization. Additionally, the weak thickness dependence of ϕ_d above the critical angle is evident. In contrast to its phase, $|e^{2i\delta}|$ in Fig 3(d) has a pronounced thickness dependence originating from the exponential dependence on d . Notably, $|e^{2i\delta}|$ and $|r_{12}|$ match only at angles above θ_c . Further, the two terms match at larger angles for lower thicknesses, qualitatively explaining the relative shifts in absorption (dispersion) with thickness in Fig 2(c). Thus, thickness can act as an additional

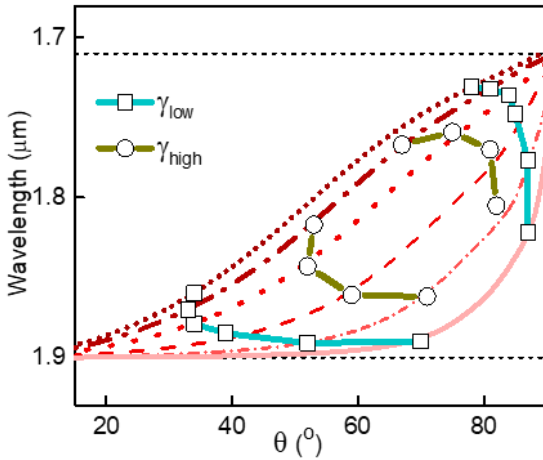


Figure 4: Loci of perfect absorption points in the $\lambda - \theta$ plane for various ENZ thicknesses and two values of loss parameter γ . Coplotted are the thickness dependent dispersions in Fig. 2(c). The low angle PA points in case of γ_{low} lie closer to λ_{ZE} than γ_{high} .

parameter for tailoring dispersion in ENZ media, in addition to the well explored carrier density tunability of the ENZ spectral range [46].

To accentuate the relevance of the ENZ media in realizing PA in ultrathin coatings, we analyze the variation in location of PA in the $\lambda - \theta$ plane (Supplementary section 9). Fig. 4 plots the PA locations for varying film thickness (20 – 400 nm) and for two values of losses (scattering rate), γ_{low} : typical value for doped CdO (squares) and γ_{high} : typical value for indium tin oxide (circles) (Supplementary sections 1). Co-plotted are the thickness dependent dispersions in Fig. 2(c), corresponding to the γ_{low} case. In general, two PA points are evidenced along a given dispersion relation, one at low angles and another at higher angles [36]. The low angle PA points lie closer to λ_{ZE} in the low loss case. A combination of low loss and low thickness in a perfect absorber may be counter-intuitive considering that a reduced absorber volume is expected to be compensated by sufficiently high loss. However, as remarked earlier, low loss PA in metal-backed ENZ layers was predicted, which require lower loss for *thinner* films [35]. To explain the low loss nature of PA in the ENZ systems shown here (Fig. 4) and in earlier works [35,54], we note that the power dissipated per unit volume in an absorbing medium is given by $P = \epsilon_0 \epsilon'' \omega |E|^2 / 2$, where ϵ_0 is the free space permittivity and E is the electric field. Clearly, any reduction in power dissipation due to the low loss may be compensated by increased electric field strengths. Consider a PEC-backed low loss thin film with vanishing ϵ_2' (Fig. 1(d)) that satisfies the zero reflectance condition for *p*-polarized light. In the absence of a reflected field in air, the incident and transmitted fields are related by the continuity relation $E_{y1} = \epsilon_2 E_{y2}$ and the field enhancement in the ENZ media is $|E_{y2}| / |E_{y1}| \approx 1/\epsilon_2''$. Thus, the field in the ENZ layer scales as $|E_2| \propto 1/\epsilon_2''$ and the resulting power absorbed per unit volume is given by $P \propto 1/\epsilon_2''$, leading to stronger absorption for lower loss in ENZ systems. This also explains why the PA points for the low loss case lie closer to λ_{ZE} than the high loss case. Figure S10 (a-e) (Supplementary section 10) shows color maps of the local field enhancement for the *y*-component of the field (E_y) with respect to the incident (background) field, at the respective PA wavelengths for three ENZ film thicknesses and two values of γ . Realization of PA is characterized by the absence of any reflected wave in air. The plots further show the variation of field enhancement across the layers (solid blue/cyan lines), which quantify the field enhancement within the ENZ layer which is highest for the thinnest film. It is worth noting that for equal thickness, the film with higher γ exhibits weaker field enhancement compared to that with lower γ . Importantly, Fig S10(f) plots the percentage of light absorbed in the Au substrate as a function of ENZ film thickness. Even for the low loss, thinnest film (20 nm), only 4% of the incident light is dissipated in the substrate with the remaining 96% absorbed by the thin film, which rises to 99% in the thicker films. Fig. S11 similarly plots the field enhancement for samples at $\lambda = 1750$ nm, away from their respective PA condition. Here, the non-zero reflectance manifests itself in the field pattern in air and the subdued field

enhancement obtained in the ENZ media. The high field enhancement at PA may be effectively exploited for a variety of applications e.g. designing high efficiency photodetectors in the relevant spectral window. Juxtaposed with the fact that the optical properties of these ENZ materials are readily tailored via chemical doping or electrical gating that tunes their $\Delta\lambda$ range, it readily opens up novel possibilities in ultrathin optical absorbers.

In conclusion, we have shown that the quarter-wave thickness limit for perfect absorption in thin films on highly metallic substrates can be surpassed employing a medium of refractive index below unity. The continuous range of interface phase shifts available on TER at the air-film interface provides the necessary phase shifts to satisfy destructive interference condition, contrasting with the conventional approach in which optical phase accumulates by light propagation in the film. Previously established constraints for achieving ultrathin film resonances such as non-trivial phase shifts at the film-substrate interface and large material loss are overcome with the help of the TER phase shift at the air-film interface, allowing destructive interference conditions to be satisfied even on PEC substrates. The proposed mechanism is importantly realized in low loss media, a unique feature distinct from previous demonstrations that used highly absorbing film or substrate materials, and is attributed to the strong ENZ field-assisted absorption. The resonant interference effects result in a well-defined modal structure restricted to incident angles above the critical angle in the low loss ENZ material CdO on an Au substrate in the near-IR range. Similar absorption features, previously observed in polaritonic materials such as phononic AlN [48] and plasmonic ITO [36], may be interpreted in terms of this interference effect. The ultrathin-film resonances described here provide design principles for perfect absorber coatings on conventional metal substrates such as Au, Al etc. without requiring complex nanostructures, and in general, will be of interest in the field of near-zero-index and thin film nanophotonics.

Acknowledgements

The authors thank Paul Dawson and Vijith Kalathingal for helpful discussions. The authors acknowledge financial support from SERB, Govt. of India (SR/52/CMP-0139/2012, CRG/2019/004965), UGC-UKIERI 184-16/2017(IC) and the Royal Academy of Engineering, Newton Bhabha Fund, UK (IAPPI_77). B.J. and S.C. acknowledge research fellowship from IISER Thiruvananthapuram.

Author contributions

B.J. developed the concept and performed the calculations. All authors contributed to analyzing and interpreting data and writing the manuscript.

Competing interests

The authors declare no competing financial interests.

References

- [1] H. A. Macleod, *Thin-film optical filters* (CRC press, 2017).
- [2] K. Kishino, M. S. Unlu, J. Chyi, J. Reed, L. Arsenault, and H. Morkoc, IEEE Journal of Quantum Electronics **27**, 2025 (1991).
- [3] M. S. Ünlü and S. Strite, Journal of Applied Physics **78**, 607 (1995).
- [4] Y. Cui, Y. He, Y. Jin, F. Ding, L. Yang, Y. Ye, S. Zhong, Y. Lin, and S. He, Laser & Photonics Reviews **8**, 495 (2014).
- [5] M. A. Kats, R. Blanchard, P. Genevet, and F. Capasso, Nature Materials **12**, 20 (2013).
- [6] M. A. Kats *et al.*, Applied Physics Letters **101**, 221101 (2012).
- [7] J. Park, J.-H. Kang, A. P. Vasudev, D. T. Schoen, H. Kim, E. Hasman, and M. L. Brongersma, ACS Photonics **1**, 812 (2014).
- [8] M. Esfandyarpour, E. C. Garnett, Y. Cui, M. D. McGehee, and M. L. Brongersma, Nature Nanotechnology **9**, 542 (2014).
- [9] J. M. Perez-Escudero, I. Buldain, M. Beruete, J. Goicoechea, and I. Liberal, Opt Express **28**, 31624 (2020).
- [10] D. Jariwala, A. R. Davoyan, G. Tagliabue, M. C. Sherrott, J. Wong, and H. A. Atwater, Nano Letters **16**, 5482 (2016).
- [11] M. A. Kats and F. Capasso, Laser & Photonics Reviews **10**, 735 (2016).
- [12] J. Rensberg *et al.*, Physical Review Applied **8**, 014009 (2017).
- [13] B. H. Woo, I. C. Seo, E. Lee, S. Y. Kim, T. Y. Kim, S. C. Lim, H. Y. Jeong, C. K. Hwangbo, and Y. C. Jun, ACS Photonics **4**, 1138 (2017).
- [14] M. ElKabbash, S. Iram, T. Letsou, M. Hinczewski, and G. Strangi, Advanced Optical Materials **6**, 1800672 (2018).
- [15] L. J. Krayer, J. Kim, and J. N. Munday, Opt. Mater. Express **9**, 330 (2019).
- [16] N. Kinsey, C. DeVault, A. Boltasseva, and V. M. Shalaev, Nature Reviews Materials **4**, 742 (2019).
- [17] O. Reshef, I. De Leon, M. Z. Alam, and R. W. Boyd, Nature Reviews Materials **4**, 535 (2019).
- [18] M. Silveirinha and N. Engheta, Physical Review Letters **97**, 157403 (2006).
- [19] M. G. Silveirinha and N. Engheta, Physical Review B **76**, 245109 (2007).
- [20] A. Alù and N. Engheta, Physical Review B **78**, 035440 (2008).
- [21] A. Alù and N. Engheta, Physical Review Letters **103**, 043902 (2009).
- [22] S. Campione, D. de Ceglia, M. A. Vincenti, M. Scalora, and F. Capolino, Physical Review B **87**, 035120 (2013).
- [23] Y. C. Jun, J. Reno, T. Ribaudo, E. Shaner, J.-J. Greffet, S. Vassant, F. Marquier, M. Sinclair, and I. Brener, Nano Letters **13**, 5391 (2013).
- [24] M. Kamandi, C. Guclu, T. S. Luk, G. T. Wang, and F. Capolino, Physical Review B **95**, 161105 (2017).
- [25] S. Enoch, G. Tayeb, P. Sabouroux, N. Guérin, and P. Vincent, Physical Review Letters **89**, 213902 (2002).
- [26] J. Kim *et al.*, Optica **3**, 339 (2016).
- [27] C. Argyropoulos, P.-Y. Chen, G. D'Aguanno, N. Engheta, and A. Alù, Physical Review B **85**, 045129 (2012).
- [28] H. Suchowski, K. O'Brien, Z. J. Wong, A. Salandrino, X. Yin, and X. Zhang, Science **342**, 1223 (2013).
- [29] T. S. Luk, D. de Ceglia, S. Liu, G. A. Keeler, R. P. Prasankumar, M. A. Vincenti, M. Scalora, M. B. Sinclair, and S. Campione, Applied Physics Letters **106**, 151103 (2015).
- [30] M. Z. Alam, I. De Leon, and R. W. Boyd, Science **352**, 795 (2016).
- [31] L. Caspani *et al.*, Physical Review Letters **116**, 233901 (2016).

- [32] A. P. Vasudev, J. H. Kang, J. Park, X. Liu, and M. L. Brongersma, *Opt Express* **21**, 26387 (2013).
- [33] Y. M. Yang, K. Kelley, E. Sachet, S. Campione, T. S. Luk, J. P. Maria, M. B. Sinclair, and I. Brener, *Nature Photonics* **11**, 390 (2017).
- [34] Y. Jin, S. S. Xiao, N. A. Mortensen, and S. L. He, *Opt. Express* **19**, 11114 (2011).
- [35] S. Feng and K. Halterman, *Physical Review B* **86**, 165103 (2012).
- [36] T. S. Luk *et al.*, *Physical Review B* **90**, 085411 (2014).
- [37] M. A. Badsha, Y. C. Jun, and C. K. Hwangbo, *Optics Communications* **332**, 206 (2014).
- [38] A. Anopchenko, L. Tao, C. Arndt, and H. W. H. Lee, *ACS Photonics* **5**, 2631 (2018).
- [39] B. T. Schwartz and R. Piestun, *J. Opt. Soc. Am. B* **20**, 2448 (2003).
- [40] B. T. Schwartz and R. Piestun, *Applied Physics Letters* **85**, 1 (2004).
- [41] A. Shahsafi, Y. Xiao, J. Salman, B. S. Gundlach, C. Wan, P. J. Roney, and M. A. Kats, *Physical Review Applied* **10**, 034019 (2018).
- [42] M. Born and E. Wolf, United Kingdom: Press Syndicate of the University of Cambridge **461** (1999).
- [43] J. Park, S. J. Kim, and M. L. Brongersma, *Opt. Lett.* **40**, 1960 (2015).
- [44] I. Liberal and N. Engheta, *Nature Photonics* **11**, 149 (2017).
- [45] E. L. Runnerstrom, K. P. Kelley, T. G. Folland, J. R. Nolen, N. Engheta, J. D. Caldwell, and J. P. Maria, *Nano Lett.* **19**, 948 (2019).
- [46] B. Johns, N. M. Puthoor, H. Gopalakrishnan, A. Mishra, R. Pant, and J. Mitra, *Journal of Applied Physics* **127**, 043102 (2020).
- [47] P. B. Johnson and R. W. Christy, *Physical Review B* **6**, 4370 (1972).
- [48] N. C. Passler, I. Razdolski, D. S. Katzer, D. F. Storm, J. D. Caldwell, M. Wolf, and A. Paarmann, *Ac_s Photonics* **6**, 1365 (2019).
- [49] H. Shen, L. Yang, Y. Jin, and S. He, *Opt Express* **28**, 31414 (2020).
- [50] B. Harbecke, B. Heinz, and P. Grosse, *Applied Physics A* **38**, 263 (1985).
- [51] S. Vassant, J. P. Hugonin, F. Marquier, and J. J. Greffet, *Opt Express* **20**, 23971 (2012).
- [52] W. D. Newman, C. L. Cortes, J. Atkinson, S. Pramanik, R. G. DeCorby, and Z. Jacob, *ACS Photonics* **2**, 2 (2014).
- [53] S. Campione, I. Brener, and F. Marquier, *Physical Review B* **91**, 121408 (2015).
- [54] J. Luo, S. Li, B. Hou, and Y. Lai, *Physical Review B* **90**, 165128 (2014).

Supplementary material for

Surpassing the quarter-wave limit for thin film perfect absorbers with epsilon-near-zero media

Ben Johns*, Shashwata Chattopadhyay & J. Mitra*

School of Physics, Indian Institute of Science Education and Research, Thiruvananthapuram, India 695551

*ben16@iisertvm.ac.in, j.mitra@iisertvm.ac.in

S1. Thin film and substrate permittivities

Dielectric function of the ENZ layer is given by a modified Drude permittivity model,

$$\epsilon_2(\omega) = \epsilon_\infty - \omega_p^2/(\omega^2 + i\omega\gamma) = \epsilon_2' + i\epsilon_2'',$$

where ω is the angular frequency, $\epsilon_\infty = 5.3$ is the background (high frequency) permittivity, $\omega_p = 2.28 \times 10^{15}$ rad/s (1.5 eV) is the plasma frequency, $\lambda_{ZE} = 1900$ nm (zero-epsilon wavelength), and $\gamma = 2.8 \times 10^{13}$ rad/s (0.018 eV) is the scattering rate, corresponding to typical values for doped CdO in this wavelength range [1].

The substrate gold (Au) is described by a Drude model approximation, $\epsilon_3(\omega) = 1 - \omega_{p,Au}^2/(\omega^2 + i\omega\gamma_{Au})$ with $\omega_{p,Au} = 1.367 \times 10^{16}$ rad/s (9 eV) and $\gamma_{Au} = 1.52 \times 10^{14}$ rad/s (0.1 eV) [2].

For the comparison of two different losses in Fig. 4 of main text, the values used are

$$\gamma_{low} = 2.8 \times 10^{13} \text{ rad/s (0.018 eV)} \text{ and } \gamma_{high} = 6 \times 10^{13} \text{ rad/s (0.04 eV).}$$

γ_{low} corresponds to typical value for CdO in this wavelength range [1].

γ_{high} corresponds to typical value for indium tin oxide (ITO) in this wavelength range [3].

S2. Eigenmode analysis

The dispersion relation for TM modes in a three medium structure is obtained as a solution (k_x, ω) of the equation [4]

$$1 + \frac{\epsilon_1 k_{z3}}{\epsilon_3 k_{z1}} = i \tan(k_{z2}d) \left(\frac{\epsilon_2 k_{z3}}{\epsilon_3 k_{z2}} + \frac{\epsilon_1 k_{z2}}{\epsilon_2 k_{z1}} \right) \quad (S1)$$

where k_x is the in-plane wave number and k_{zi} the transverse wave number in medium $i = 1,2,3$, which are related by $k_{zi}^2 = \epsilon_i \omega^2 / c^2 - k_x^2$. A real k_x and complex ω representation is chosen here, in accordance with previous numerical studies on such systems [5,6]. See also supplementary section 9. Fig 2(c) in the main text is plotted by in the $\theta - \lambda$ plane using the relations $\omega = 2\pi c / \lambda$ and $k_x = (2\pi / \lambda) \sin \theta$.

S3. Supplementary reflectance plots

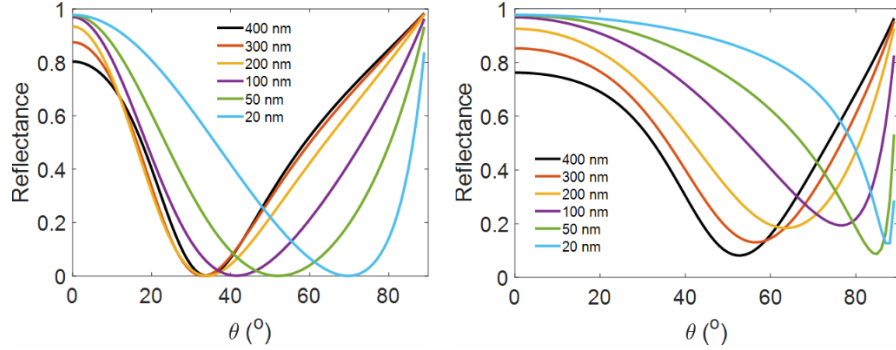


Figure S1: Reflectance vs angle for ENZ (doped CdO) thin films of varying thickness on Au at (a) respective PA wavelengths (b) at $\lambda = 1800$ nm, corresponding to horizontal line cuts of the data presented in figure 2(d-i) of main text.

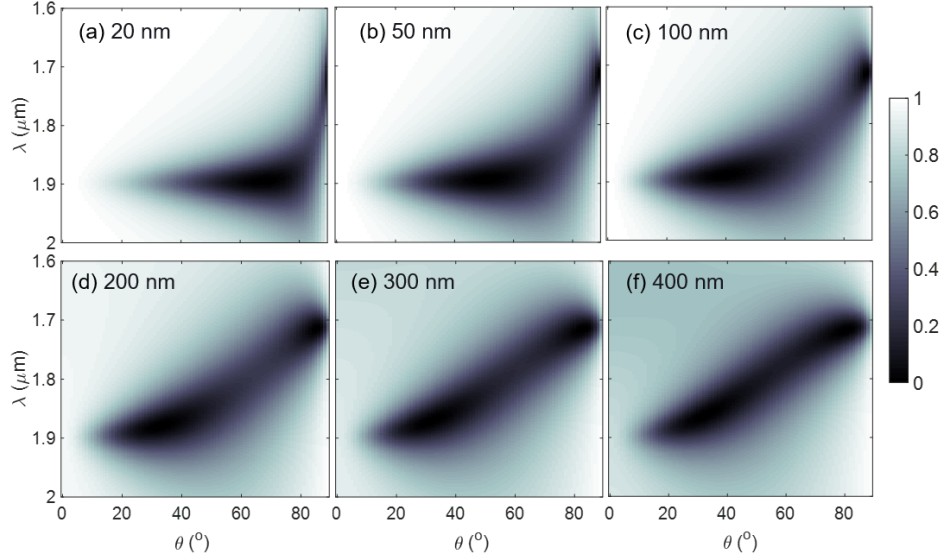


Figure S2: Reflectance of doped CdO films of varying thickness on a perfect electric conductor (PEC), i.e. $r_{23} = -1$, showing absorption features similar to that obtained with an Au substrate shown in Fig 2 in main text.

S4. Fabry-Perot modes in doped CdO on Au at lower wavelengths

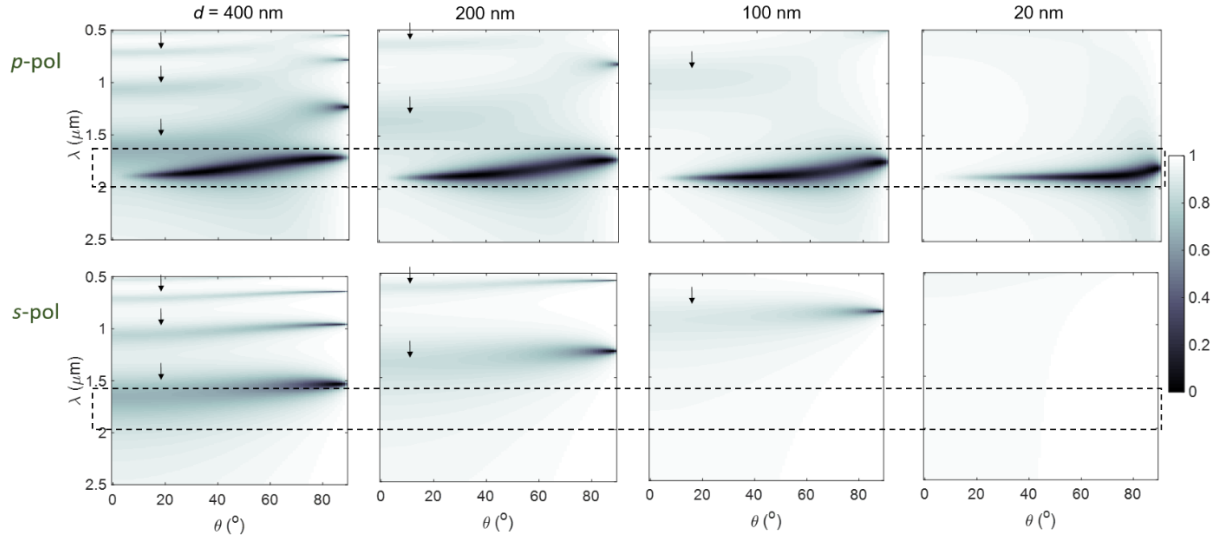


Figure S3: Reflectance maps in Fig 2 of main text are shown here for an extended wavelength range from 500 – 2500 nm for *p*- (top) and *s*-polarization (bottom panels). Quarter-wave and higher order Fabry-Perot modes are indicated by arrows. For the thickest film ($d = 400$ nm), conventional Fabry-Perot modes are seen at low wavelengths for both polarizations (dark regions). With decreasing thickness, the modes move to lower wavelengths and finally disappear, leaving only the absorption of *p*-polarized light in the ENZ regime. The boxes show the range of wavelengths presented in the main text.

S5. Reflectance and dispersion of thicker films ($d > 400$ nm)

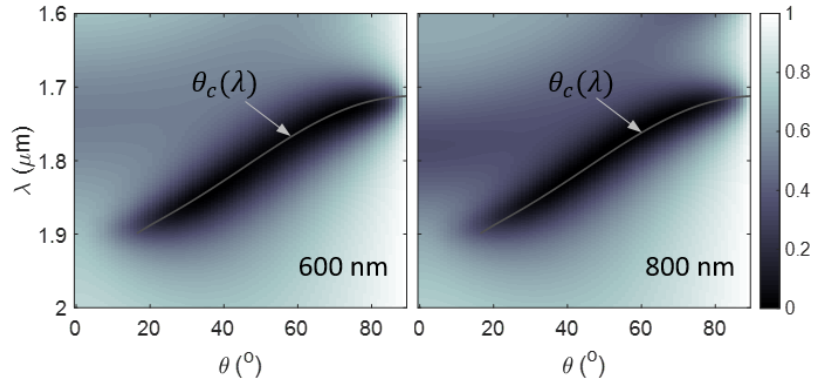


Figure S4: Fig 2 in main text plots reflectance of ENZ layer on Au up to $d = 400$ nm. Reflectance for thicker films is shown here ($d = 600, 800$ nm) clearly revealing that the absorption profile is limited by the critical angle at higher thicknesses (solid line). Fabry-Perot modes also start appearing within the $\Delta\lambda$ range at these thicknesses, as evidenced by light grey areas towards the short wavelength side.

S6. Contrast with polaritonic modes

The frequency and wave vector (ω, k) of a surface polariton at the interface of a polaritonic medium with air are related by $k^2 = \frac{\epsilon(\omega)}{1+\epsilon(\omega)} \frac{\omega^2}{c^2}$, where $\epsilon(\omega)$ is the permittivity of the medium [7]. For $\epsilon(\omega) > 0$, $k^2 < \omega^2/c^2$, which means that the dispersion in the dielectric regime ($\lambda < \lambda_{ZE}$) always lies to the left of the light line in air. Therefore, the radiative polaritonic dispersion does not approach the light line at any wavelength. This is in contrast to the dispersion in an asymmetric, metal-backed structure (Fig. 2 in main text) where the modes approach the light line ($\theta_1 = 90^\circ$) within the $\Delta\lambda$ range.

‘ENZ modes’ are polaritonic surface modes supported in ultrathin ENZ films in a symmetric or asymmetric dielectric environment or even on a metallic substrate [4,8,9]. They feature a predominantly flat dispersion on either side of the light line at the zero permittivity frequency and are attributed to the excitation of bulk polaritons in films much thinner than the skin depth [10]. However, in relatively thicker films, the modes no longer lie at the zero permittivity frequency and we may expect the optical environment to play a prominent role in deciding their dispersion relations. For example, in the case of a metallic film in a symmetric environment, the ENZ mode evolves into long-range surface plasmon polaritons (SPPs) with increasing thickness. In contrast, long-range SPPs are not supported in an asymmetric dielectric environment. Therefore, it is reasonable to assume that the modes in a *metal-backed* configuration may

have features or origin distinct from their symmetric counterparts owing to the asymmetric optical environment.

As evident from the dispersion relations and reflectance maps in Fig. 2 of the main text, the thinnest film with $d = 20 \text{ nm} \approx \lambda/50$ indicates polaritonic Berreman mode (radiative ENZ mode) excitation, with a predominantly flat absorption profile at λ_{ZE} . The dispersions progressively blue-shift with increasing film thickness and have a qualitatively different shape for larger thicknesses, becoming nearly identical as they are limited by the wavelength-dependent critical angle. To show that our predictions are independent of polaritonic or ENZ effects and depend only on TIR at the top interface, we calculated the reflectance of an analogous system. Here, the ENZ layer is replaced with an air gap ($n_2 = 1$) and the top dielectric medium is chosen to have $n_1 > 1$ so that it ensures the possibility of TIR while precluding ENZ effects in the thin film layer. The top panel in Fig. S5 shows the calculated reflectance vs θ at three wavelengths in the $\Delta\lambda$ range (1750, 1800 and 1850 nm) for various ENZ thicknesses, corresponding to horizontal line cuts of the plots in Fig. S2. Evidently, reflection minima appear only above θ_c , marked by dashed vertical lines. Now, in the second system with an air gap between a higher index dielectric and PEC substrate, n_1 is chosen such that the critical angle at the dielectric-air interface, $\theta_c = \sin^{-1} n_2/n_1$, remains the same as in the ENZ on PEC case (Fig S5, bottom panel). For example, at $\lambda = 1800 \text{ nm}$, the ENZ refractive index $n_2 = 0.74$, corresponding to $\theta_c = \sin^{-1} 0.74/1 = 48^\circ$. In the corresponding second system, the refractive indices are chosen such that $\theta_c = \sin^{-1} 1/n_1 = 48^\circ$, giving $n_2 = 1.34$. Indeed, the reflection minima again appear above the critical angle, showing similar reflection dips as in the top panel.

Note that although the second system is analogous to the Otto configuration, the reflection dips do not arise from surface plasmon excitation as the PEC substrate does not support any surface waves.

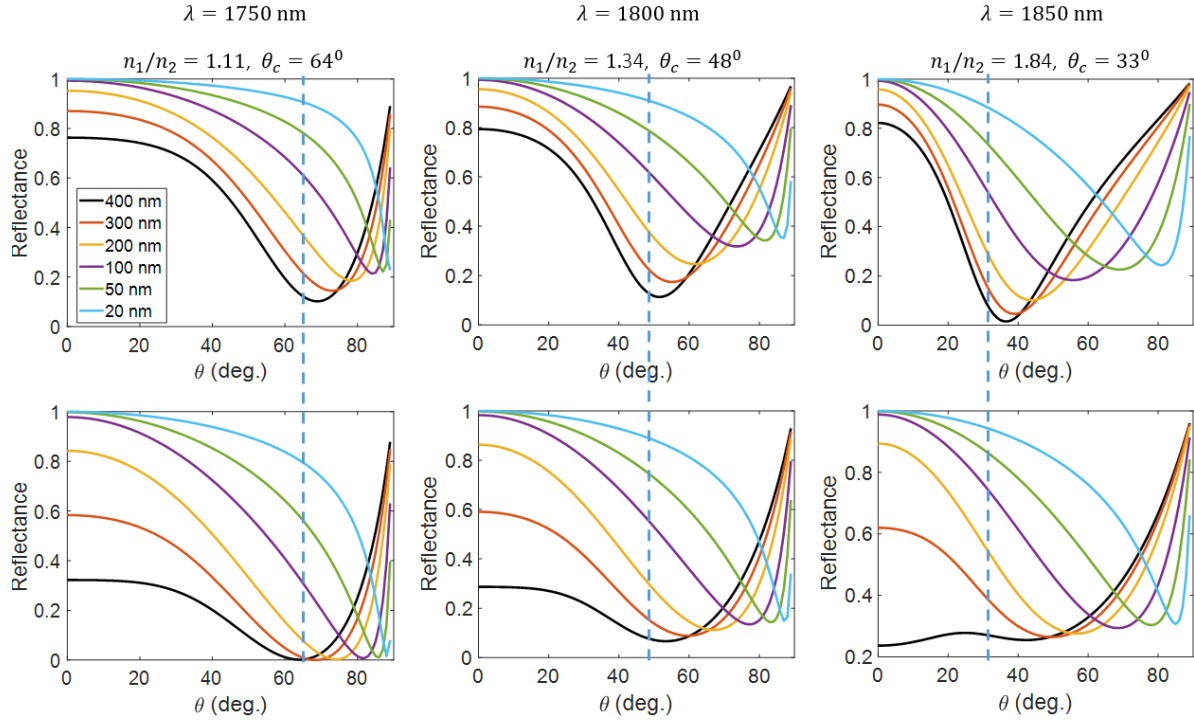


Figure S5: Calculated reflectance vs angle of incidence for Air:ENZ:PEC (top) and dielectric:air gap:PEC (bottom). The wavelengths, refractive indices and critical angles are noted. Dashed vertical lines denote the critical angle, above which reflection minima are seen in both systems.

S7. Asymmetric FP cavity

The polarization-dependent Fresnel reflection coefficients r_{ij} at an interface of media i and j are given by [11]

$$r_{ij} = \frac{\epsilon_i k_{zj} - \epsilon_j k_{zi}}{\epsilon_i k_{zj} + \epsilon_j k_{zi}} \quad (p\text{-polarization}) \quad (\text{S2})$$

$$r_{ij} = \frac{k_{zi} - k_{zj}}{k_{zi} + k_{zj}} \quad (s\text{-polarization}) \quad (\text{S3})$$

Where k_{zi} (or k_{zj}) is the normal wave vector component in medium i (or j). For zero total reflectance, eqn. 1 in main text requires that two relations must be satisfied simultaneously:

$$\phi_{12} - (\phi_{23} + \phi_d) = (2m + 1)\pi \quad (S4)$$

$$|r_{12}| = |r_{23}e^{2i\delta}| = |r_{23}|e^{-2d \operatorname{Im}(k_{z2})} \quad (S5)$$

where $r_{ij} = |r_{ij}|e^{i\phi_{ij}}$, ϕ_{ij} are reflection phase shifts, $\phi_d = 2d \operatorname{Re}(k_{z2})$ is the propagation phase accumulated by a roundtrip in the film and m is an integer. A reflectance minimum is observed when these two equations are approximately satisfied.

For a PEC substrate, $r_{23} = -1$. This simplifies the above two equations to:

$$\phi_{12} = \phi_d + 2m\pi \quad (S6)$$

$$|r_{12}| = |e^{2i\delta}| = e^{-2d \operatorname{Im}(k_{z2})} \quad (S7)$$

For the case of $n_2 < 1$ such as an ENZ or NZI medium, above the critical angle, the reflection phase shifts are angle dependent [Fig. S6(a)], given by:

$$\phi_{12(p)} = 2 \tan^{-1} \frac{n\sqrt{n^2 \sin^2 \theta_1 - 1}}{\cos \theta_1} \quad (\phi_{12}, p\text{-polarization}) \quad (S8)$$

$$\phi_{12(s)} = 2 \tan^{-1} \frac{\sqrt{n^2 \sin^2 \theta_1 - 1}}{n \cos \theta_1} \quad (\phi_{12}, s\text{-polarization}) \quad (S9)$$

where $n = \frac{n_1}{n_2}$. Fig. S6(b) plots the magnitude of r_{12} given by eqn. S7.

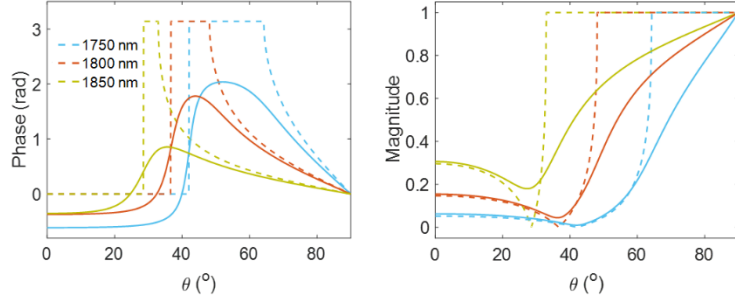


Figure S6: Reflection phase ϕ_{12} (a) and magnitude $|r_{12}|$ (b) versus angle of incidence for p -polarized light incident at the air-ENZ interface, at wavelengths $\lambda = 1750, 1800$ and 1850 nm corresponding to critical angles $\theta_c = 64^\circ, 48^\circ$ and 33° . The dashed lines show the lossless case, setting $k_2 = 0$. The continuous variation of ϕ_{12} above critical angle in (a) is described by eqn. S8. Solid lines show calculations with loss that are numerically evaluated from eqn. S2. The sharp variation in $|r_{12}|$ at angles near the critical angle is clear in the lossless case in (b), while the presence of loss prevents complete (unity) reflection above the critical angle (solid lines).

Fig. 3 in main text compares the phases and magnitudes of the terms in eqns. S6 and S7 at $\lambda = 1800$ nm.

Fig. S7 compares r_{12} and $e^{2i\delta}$ for three wavelengths in the $\Delta\lambda$ range viz. 1750, 1800 and 1850 nm.

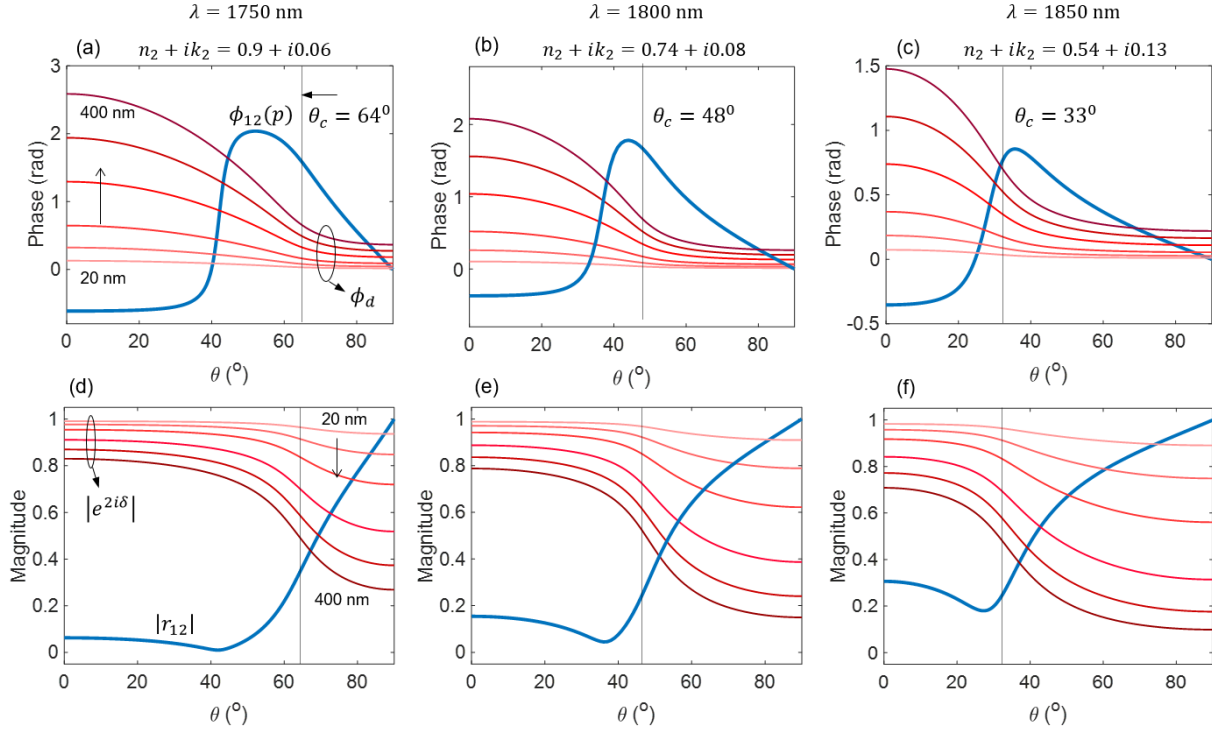


Figure S7: Comparison of phases (a-c) and magnitudes (d-f) of r_{12} and $e^{2i\delta}$ for the ENZ layer, showing the intersection points where eqns. S6 and S7 are satisfied. From left to right, vertical panels correspond to wavelengths $\lambda = 1750$ nm, 1800 nm and 1850 nm respectively. In general, the phases match in two angle ranges: one below the critical angle and one at larger angles. However, the magnitudes match only above the critical angle (vertical lines) as seen in the bottom panel, restricting the absorption to angles above θ_c .

S8. Interference picture using transfer matrix field formulation

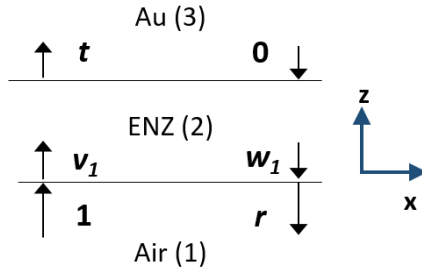


Figure S8: Schematic representation of counter-propagating fields in the three-medium system. Arrows show direction of propagation of waves and the corresponding amplitudes are marked next to each arrow.

To analyze multilayer structures, it is useful to treat the waves in each layer as having a forward (+z) and backward (-z) moving component as shown schematically in Fig. S6. The forward (backward) moving

wave in each layer is the sum of infinitely many forward (backward) moving partial waves in the partial wave picture [12]. The fields in each layer can be related by the two expressions,

$$v_{n+1} = v_n e^{i\delta_n} t_{n,n+1} + w_{n+1} r_{n+1,n}$$

$$w_n = w_{n+1} t_{n+1,n} e^{i\delta_n} + v_n r_{n,n+1} e^{2i\delta_n}$$

where n is the number of interfaces, $\delta_n = k_{zn} d_n$, the product of perpendicular wave number and thickness in layer n . This allows us to intuitively breakdown the total multilayer reflectance r into two components: the initial incident wave reflected at the first interface r_{12} , and the forward propagating wave in medium 2 (w_1) that is transmitted into medium 1. We then get $r = 1 \times r_{12} + w_1 \times t_{21}$, where the second term $w_1 t_{21}$ is the resultant sum of all partial waves originating from the thin film. Thus, destructive interference effects depend on these two waves cancelling each other out, which we refer to as direct and indirect pathways respectively. The direct pathway amplitude is simply $E_{direct} = r_{12}$. The complex amplitude in the indirect pathway may be written as

$$E_{indirect} = w_1 \times t_{21} = \frac{r_{23}(1 - r_{12}^2)}{r_{12}r_{23} + e^{-2i\delta}} = r_{23}e^{2i\delta}(1 - r_{12}r) = -e^{2i\delta}(1 - r_{12}r)$$

Note that at $r = 0$, $E_{indirect} = -e^{2i\delta}$. Therefore, comparing and equating the terms r_{12} and $e^{2i\delta}$ as done in the main text may be interpreted as the condition for destructive interference between the direct and indirect pathways in the multilayer system.

S9. Analysis of perfect absorption

While various complementary descriptions may be used to analyze perfect absorption in the system, we use the formalism of Luk et al [5] to identify PA locations from the eigenmode analysis described in supplementary section 2. From the real wave number–complex frequency solutions of the dispersion relation in eqn. S1, the condition for PA is a zero imaginary part of ω , i.e. $Im(\omega) = 0$. A positive (negative) imaginary part of the mode frequency corresponds to growing (decaying) fields in the structure. The sign of k_{z1} is chosen such that it always corresponds to an incoming wave in medium 1 (air). A zero imaginary part thus corresponds to an incoming plane wave in the first medium that is completely absorbed in the structure without any reflection. Figure S9 (a, b) shows the trajectory of modes in the complex frequency plane i.e. $Im(\omega)$ vs $Re(\omega)$ for thicknesses from 20 nm to 400 nm for $\gamma_{low} = 2.8 \times 10^{13}$ and $\gamma_{high} = 6.0 \times 10^{13}$ rad/s respectively. The PA locations are identified where the trajectories cross the x-axis, which agree well with the reflectance minima extracted numerically from eqn. 1 in the main text.

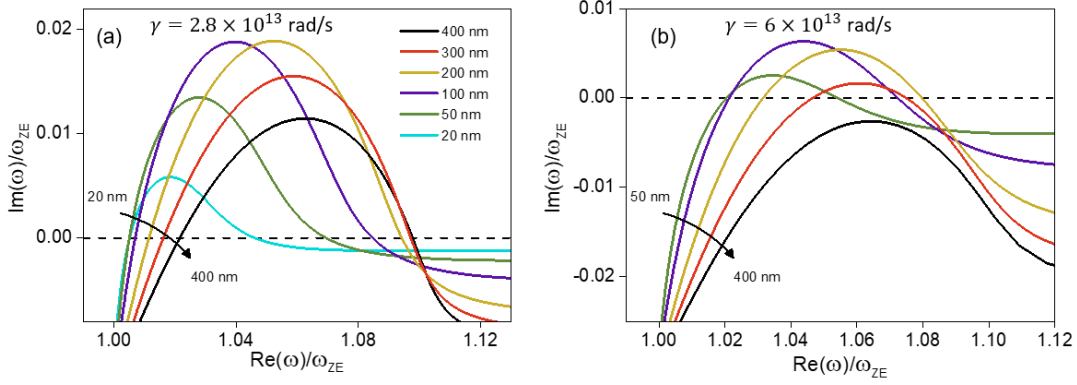


Figure S9: Plots of $Im(\omega)$ vs $Re(\omega)$ normalized to ω_{ZE} for (a) $\gamma_{low} = 2.8 \times 10^{13}$ rad/s and (b) $\gamma_{high} = 6 \times 10^{13}$ rad/s. In general, the trajectories cross the x-axis at two values of $Re(\omega)$, denoting two PA locations. To plot the corresponding PA points in the $\lambda - \theta$ plane shown in Fig. 4 of main text, the values of $Re(\omega)$ are used to identify the corresponding θ values from the respective dispersion relations. In (a), all the thicknesses have two PA locations while in (b), no PA condition is possible for the thickest film ($d = 400$ nm), which does not cross the x-axis in this frequency range.

S10. Field profiles at and away from the PA condition

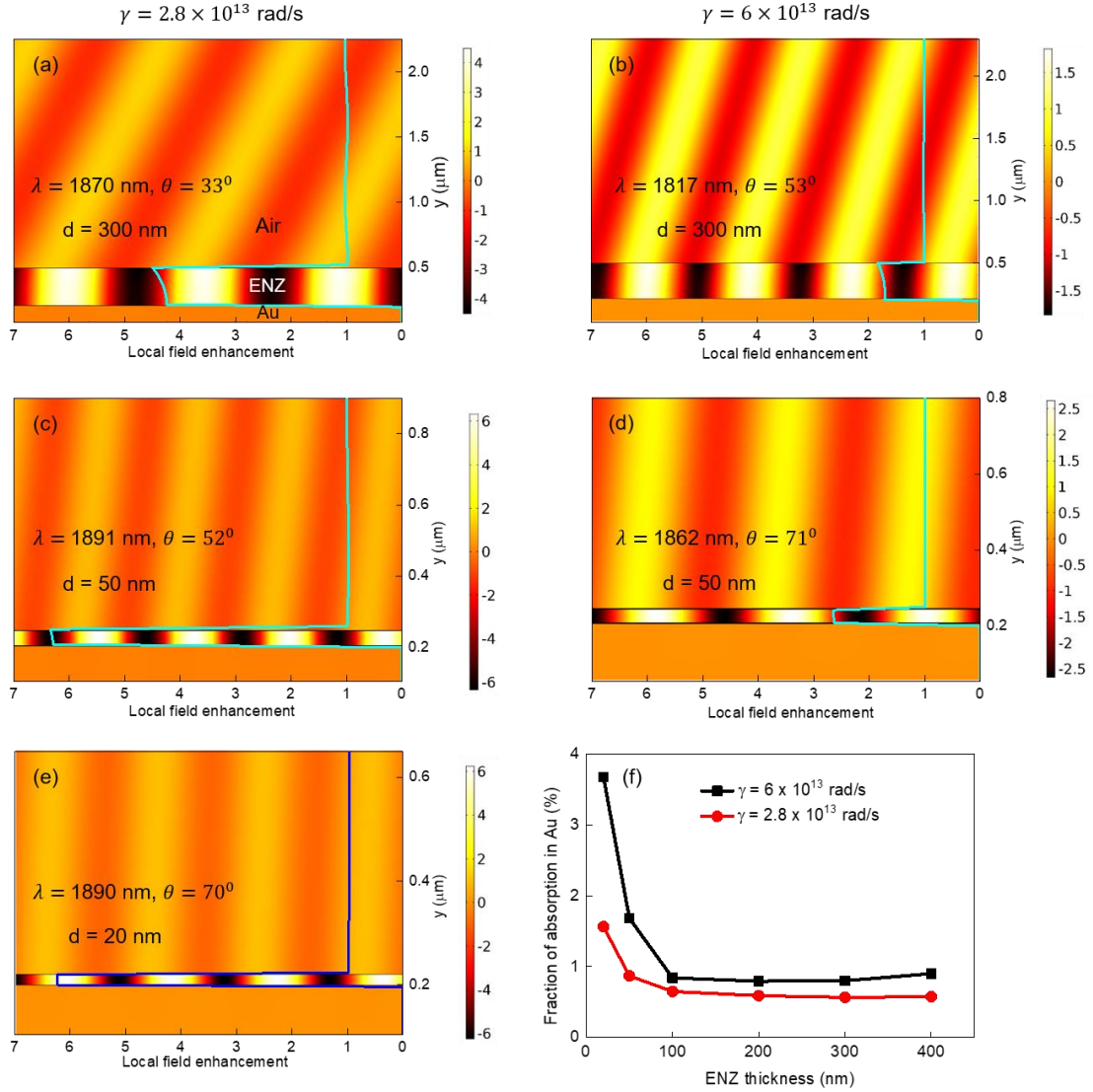


Figure S10: (a-e) Electric field distribution in the ENZ:M system for various ENZ film thickness and two losses at their respective PA conditions (see text inset and Fig. 4 in main text). Solid cyan/blue lines plot $|E_y|$ enhancement across the 3 layers, overlaid on its spatial profile (color map) showing local electric field strength in the three media. Spatial field variation in air is characterized by the absence of any outgoing reflected wave due to PA. Higher $|E_y|$ in the ENZ layer is achieved for the lower loss case, determined by the absolute value of permittivity at the PA wavelength. (f) Percentage of the energy absorbed in the Au substrate for various ENZ thickness for the two losses.

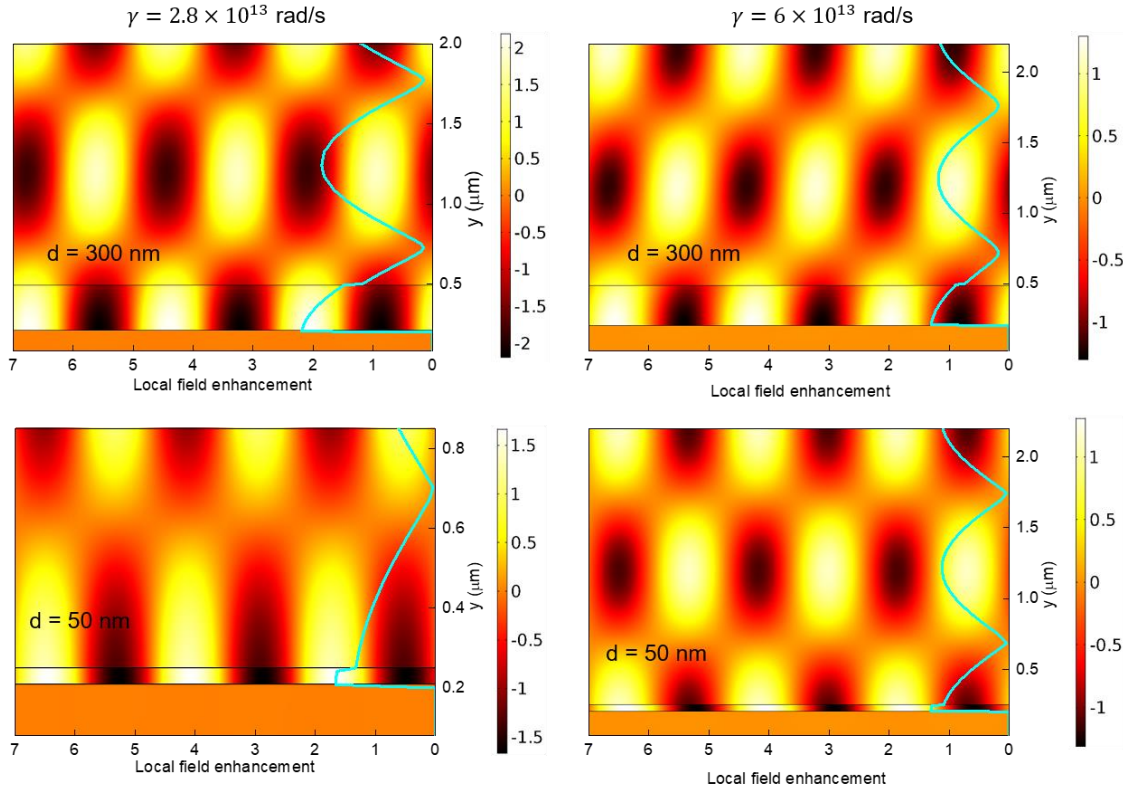


Figure S11: Variation in enhancement of $|E_y|$ across the 3 layers for $\lambda = 1750$ nm and $\theta = 33^\circ$ (away from PA conditions) for two different thickness and loss values. In contrast to Fig S10, field profiles in air clearly reveal superposition of counter-propagating waves (incident and reflected).

References

- [1] E. L. Runnerstrom, K. P. Kelley, T. G. Folland, J. R. Nolen, N. Engheta, J. D. Caldwell, and J. P. Maria, *Nano Lett* **19**, 948 (2019).
- [2] A. D. Rakić, A. B. Djurišić, J. M. Elazar, and M. L. Majewski, *Appl. Opt.* **37**, 5271 (1998).
- [3] B. Johns, N. M. Puthoor, H. Gopalakrishnan, A. Mishra, R. Pant, and J. Mitra, *Journal of Applied Physics* **127**, 043102 (2020).
- [4] S. Campione, I. Brener, and F. Marquier, *Physical Review B* **91**, 121408 (2015).
- [5] T. S. Luk *et al.*, *Physical Review B* **90**, 085411 (2014).
- [6] N. C. Passler, I. Razdolski, D. S. Katzer, D. F. Storm, J. D. Caldwell, M. Wolf, and A. Paarmann, *Acs Photonics* **6**, 1365 (2019).
- [7] D. L. Mills and E. Burstein, *Reports on Progress in Physics* **37**, 817 (1974).
- [8] B. Harbecke, B. Heinz, and P. Grosse, *Applied Physics A* **38**, 263 (1985).
- [9] S. Vassant, J. P. Hugonin, F. Marquier, and J. J. Greffet, *Opt Express* **20**, 23971 (2012).
- [10] T. Tyborski, S. Kalusniak, S. Sadofev, F. Henneberger, M. Woerner, and T. Elsaesser, *Phys Rev Lett* **115**, 147401 (2015).
- [11] D. J. Griffiths, *Introduction to electrodynamics* (Prentice Hall, 2005).
- [12] P. Yeh, *Optical Waves in Layered Media* (John Wiley & Sons, 2005).